Nonlinear Vibration Analysis of Turbine Bladed Disks with Midspan Dampers

Journal of Engineering for Gas Turbines and Power

# NONLINEAR VIBRATION ANALYSIS OF TURBINE BLADED DISKS WITH MID-SPAN DAMPERS

**Erhan Ferhatoglu[1], Stefano Zucca[1], Daniele Botto[1], Jury Auciello[2], Lorenzo Arcangeli[2]**

[1] Department of Mechanical and Aerospace Engineering, Politecnico di Torino, Italy
[2] Baker Hughes, Turbomachinery and Process Solution, Florence, Italy

## ABSTRACT

Friction dampers are one of the most common secondary structures utilized to alleviate excessive vibration amplitudes in turbomachinery applications. In this paper, the dynamic behavior of the turbine bladed disks coupled with one of the special damper designs, the so-called Mid-Span Dampers (MSDs) that is commonly used in steam turbines of Baker Hughes Company, is thoroughly studied. Friction between the blade and the damper is modeled through a large number of contact nodes by using 2D contact elements with a variable normal load. In the solution procedure, the coupled static/dynamic Harmonic Balance approach is utilized for the first time in the assessment of the dissipation capability of MSDs, computationally shown by predicting the forced response levels of the system at different resonances. Moreover, it is demonstrated that the nonlinear dynamic response is non-unique and it may vary considerably even if all the user-controlled inputs are kept identical. This phenomenon is a novel observation for MSDs and it is explained by an uncertainty present in the contact forces. Contact conditions corresponding to multiple responses are also investigated to unveil the different kinematics of the damper under the same nominal conditions.

Keywords: Nonlinear Vibration, Friction Damping, Turbine Blades, Response Variability, Non-unique Contact Forces

## 1. INTRODUCTION

High vibration amplitudes in turbine blades may cause severe problems such as high cycle fatigue failure [1, 2]. Necessary precautions are taken into account during the design stage in order to prevent undesired situations.

One of the most appropriate solution methods to reduce dynamic response amplitudes is to avoid resonance regions with blade detuning. Despite the high effectiveness of this approach, changing the natural frequency values of the turbomachinery parts is not too easy due to their high modal density and the wide spectrum of the external excitation force. Another efficient technique is to utilize the dry friction damping technologies by deliberately implementing contact pairs into the turbine blades in order to dissipate the excessive energy. Some examples of the use of contacts are at the blade-disk interfaces [3, 4], at the shrouds on the blade tip [5, 6] or with ring dampers [7, 8] and friction dampers located under the blade platforms [9-12]. Mid-Span Damper (MSD) is also a special type of friction dampers, which is extensively used at the Last Stage Blades (LSBs) of Baker Hughes' steam turbines. In this paper, we performed an elaborate investigation on the dynamic behavior of LSBs coupled with MSDs.

LSBs have very low stiffness due to their relatively thin airfoils with complex 3D shapes. Moreover, LSBs are exposed to very large centrifugal and aerodynamic forces during operation, which makes them to operate in a very severe condition [13]. This requires a special type of friction dampers to be utilized and MSDs are particularly designed for LSBs. The design of MSDs is historically based on a more traditional damping wire configuration in which a wire passes through a hole located on the blade [14]. The geometry of MSDs is slightly different than those of other dampers, very well-known in the literature, such as under-platform dampers [9-12]. MSDs are metal devices with different design shapes such as pin or sleeve geometry. Figure 1 representatively shows bladed disks coupled with the pin geometry of MSDs which are placed approximately at 70% of the airfoil span and come into contact with LSBs by the centrifugal force acting during rotation. In the literature, MSDs are also known as the so-called friction bolt damping element [15, 16]. Nonlinear vibration analyses of LSBs with integral connections have been conducted in [17, 18] and it has been shown that friction damping plays an important role for LSBs to be able to reduce stress levels and vibration amplitudes.

In this study, a thorough investigation on the nonlinear dynamic assessment of LSBs coupled with MSDs is performed. MSD is modeled with free-free boundary conditions where it exhibits six rigid body modes and several elastic modes. Only constraint between the blade and damper is friction contacts that are achieved through a large contact patch by utilizing 2D contact elements with a variable normal load. Differently from the previous studies, there are three main novel parts in this study. Firstly, dynamic response amplitudes are obtained through the use of the coupled static/dynamic Harmonic Balance approach. Unlike the previous studies, the $0^{th}$ order harmonic is included in the solution procedure and this ensures the computation of more accurate results [19]. Secondly, the dynamic response variability under the same nominal conditions is shown as the first time in LSBs coupled with MSDs. To explain the variability phenomenon, the damper kinematics is deeply studied by investigating the contact status

of each element for different responses. It is demonstrated that multiple responses are due to an uncertainty related to the non-uniqueness of friction forces [20]. Finally, the dissipation capability of MSDs is shown in different resonance regions with a large amount of excitation levels and pre-loads. This can be considered as the most intensive investigation on the nonlinear vibration analyses of LSBs with MSDs. We show that MSDs are highly capable of introducing friction damping in LSBs, which helps to decrease large vibration amplitudes.

The paper is organized as follows. Section 2 introduces the theoretical background of bladed disk dynamics with MSDs. Section 3 shows an abundant amount of results with dynamic response amplitudes, the variability phenomenon and the damper kinematics. Section 4 summarizes and concludes the paper.

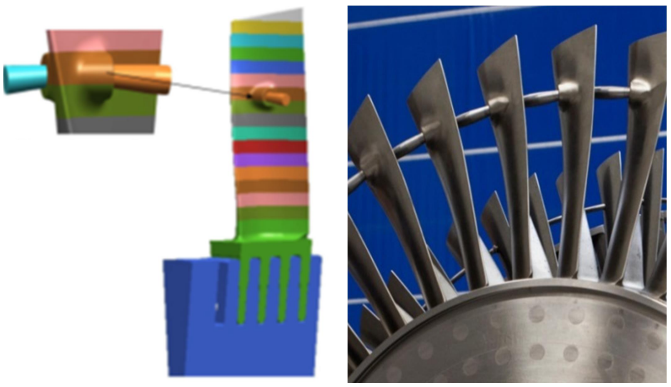

**FIGURE 1**: MID-SPAN DAMPERS WITH BLADED DISKS.


## 2. THEORETICAL BACKGROUND OF BLADED DISK DYNAMICS WITH MID-SPAN DAMPERS

### 2.1 Governing Equation of Motion

Bladed disks consist of $N_s$ number of theoretically identical sectors under the assumption of tuned conditions and they are exposed to a travelling wave excitation. Each sector is divided evenly over a $2\pi$ angle and the dynamic behavior of the entire bladed disk can be inferred with cyclic symmetry [21] by studying on only one fundamental sector that is composed of one LSB and one MSD.

The differential equation of the motion for the fundamental sector under a periodic excitation in time domain can be written as

$$\mathbf{M}\ddot{\mathbf{q}}(t)+\mathbf{C}\dot{\mathbf{q}}(t)+\mathbf{K}\mathbf{q}(t)+\mathbf{f}_n(\mathbf{q},\dot{\mathbf{q}},t)=\mathbf{f}_{ex}(t)\,, \tag{1}$$

where $\mathbf{M}$, $\mathbf{C}$ and $\mathbf{K}$ are the mass, viscous damping and stiffness matrices of the linear system, respectively. $\mathbf{q}(t)$ represents the vector of generalized coordinates. $\mathbf{f}_{nl}(\mathbf{q},\dot{\mathbf{q}},t)$ and $\mathbf{f}_{ex}(t)$ are the vector of internal nonlinear contact force and the vector of external periodic force, respectively. Dot denotes derivative with respect to time $t$.

Periodic excitation force can be decomposed to its harmonic components as

$$\mathbf{f}_{ex}(t)=\hat{\mathbf{f}}_{ex}^{0}+\Im\left(\sum_{h=1}^{H}\hat{\mathbf{f}}_{ex}^{eo\cdot h}e^{ih\omega t}\right)\,. \tag{2}$$

Here, $eo$ is the fundamental engine order of the travelling wave excitation. $\hat{\mathbf{f}}_{ex}^{0}$ and $\hat{\mathbf{f}}_{ex}^{eo\cdot h}$ are the real and complex amplitude vectors of the $0^{\text{th}}$ and the $eo\cdot h^{\text{th}}$ harmonics, respectively. $H$ is the number of harmonics considered in the expansion. $i$ represents the imaginary unit number. $\omega=eo\cdot\Omega$, being $\Omega$ is the rotation speed of the rotor hub.

In steady state conditions, periodic excitation force determines periodic response and periodic contact forces that can be written as

$$\mathbf{q}(t)=\hat{\mathbf{q}}^{0}+\Im\left(\sum_{h=1}^{H}\hat{\mathbf{q}}^{eo\cdot h}e^{ih\omega t}\right)\,, \tag{3}$$

$$\mathbf{f}_n(t)=\hat{\mathbf{f}}_n^{0}+\Im\left(\sum_{h=1}^{H}\hat{\mathbf{f}}_n^{eo\cdot h}e^{ih\omega t}\right)\,, \tag{4}$$

where $\hat{\mathbf{q}}^{eo\cdot h}$ and $\hat{\mathbf{f}}_n^{eo\cdot h}$ are the complex amplitude vectors of the response and contact forces corresponding to the $eo\cdot h^{\text{th}}$ harmonics, respectively. $\hat{\mathbf{q}}^{0}$ and $\hat{\mathbf{f}}_n^{0}$ represent the real bias amplitude vectors of the response and contact forces, respectively. Substituting Eqs. (2), (3) and (4) into Eq. (1), the following set of nonlinear algebraic equations in frequency domain can be obtained

$$\begin{gathered}\mathbf{K}^{0}\hat{\mathbf{q}}^{0}+\hat{\mathbf{f}}_n^{0}-\hat{\mathbf{f}}_{ex}^{0}=\mathbf{0}\\ \left(\mathbf{K}^{eo\cdot h}-(h\omega)^{2}\mathbf{M}^{eo\cdot h}+ih\omega\mathbf{C}^{eo\cdot h}\right)\hat{\mathbf{q}}^{eo\cdot h}+\hat{\mathbf{f}}_n^{eo\cdot h}-\hat{\mathbf{f}}_{ex}^{eo\cdot h}=\mathbf{0}\quad(h=1,\cdots,H)\end{gathered} \tag{5}$$

In Eq. (5), superscript $eo\cdot h$ referring to system matrices means that cyclic symmetry boundary conditions corresponding to the $eo\cdot h^{\text{th}}$ harmonic must be enforced.

### 2.2 Cyclic Symmetry and Reduced Order Model

The complex amplitude vector of the fundamental sector, $\hat{\mathbf{q}}^{eo\cdot h}$, can be separated into three groups as $\hat{\mathbf{q}}^{eo\cdot h}=\left[\left({}_{l}\hat{\mathbf{q}}^{eo\cdot h}\right)^{T},\left({}_{i}\hat{\mathbf{q}}^{eo\cdot h}\right)^{T},\left({}_{r}\hat{\mathbf{q}}^{eo\cdot h}\right)^{T}\right]^{T}$, where superior $T$ is the transpose operator. ${}_{l}\hat{\mathbf{q}}^{eo\cdot h}$ and ${}_{r}\hat{\mathbf{q}}^{eo\cdot h}$ are the sector interface nodes lying on the left and right side, respectively, while ${}_{i}\hat{\mathbf{q}}^{eo\cdot h}$ is the remaining interior nodes. It should be noted that ${}_{l}\hat{\mathbf{q}}^{eo\cdot h}$ and ${}_{r}\hat{\mathbf{q}}^{eo\cdot h}$ are cyclically symmetric in tuned bladed disks and cyclic symmetry boundary conditions can be imposed to the fundamental sector interfaces as [21]

$$\hat{\mathbf{q}}^{eo\cdot h} = \begin{Bmatrix} {}_l\hat{\mathbf{q}}^{eo\cdot h} \\ {}_i\hat{\mathbf{q}}^{eo\cdot h} \\ {}_r\hat{\mathbf{q}}^{eo\cdot h} \end{Bmatrix} = \underbrace{\begin{bmatrix} \mathbf{I} & \mathbf{0} \\ \mathbf{0} & \mathbf{I} \\ \mathbf{I}e^{i\varphi eo\cdot h} & \mathbf{0} \end{bmatrix}}_{\mathbf{T}^{eo\cdot h}} \begin{Bmatrix} {}_l\hat{\mathbf{q}}^{eo\cdot h} \\ {}_i\hat{\mathbf{q}}^{eo\cdot h} \end{Bmatrix}, \quad (6)$$

where $\varphi$ is the inter-blade phase angle, i.e. $\varphi = 2\pi/N_s$. $\mathbf{T}^{eo\cdot h}$ is the transformation matrix and it can be used to obtain cyclically symmetric system matrices, which is given in Eq. (5), as

$$\mathbf{K}^{eo\cdot h} = \left(\mathbf{T}^{eo\cdot h}\right)^* \mathbf{K}\mathbf{T}^{eo\cdot h} \qquad \mathbf{M}^{eo\cdot h} = \left(\mathbf{T}^{eo\cdot h}\right)^* \mathbf{M}\mathbf{T}^{eo\cdot h}$$
$$\mathbf{C}^{eo\cdot h} = \left(\mathbf{T}^{eo\cdot h}\right)^* \mathbf{C}\mathbf{T}^{eo\cdot h}, \quad (7)$$

where superior * is the Hermitian operator.

The use of cyclic symmetry largely reduces the size of the models; however, the number of Degrees of Freedoms (DOFs) even for one sector may be unmanageably large and needs to be decreased. Component Mode Synthesis (CMS) techniques are used to further reduce the model order to a reasonable level.

One of the very-well known CMS methods, which is applied in this study, is the Craig-Bampton (CB) reduction approach [22]. According to the CB [22], the system DOFs are divided into two groups as the master and slave coordinates and a reduced order model (ROM) is constructed from the fundamental sector through the use of a transformation matrix. The master DOFs are selected as the physical contact nodes, force application nodes, response monitoring nodes and modal coordinates associated with the specific number of linear modes chosen by the user. The details about the theory of the CB are not presented here for brevity and more information can be found in [22]. It should also be noted that Eq. (5) refers to DOFs of the ROM, after obtaining the ROM matrices with the CB approach.

### 2.3 Contact Elements and Computation of Friction Forces

The friction is modeled by using a node-to-node 2D Jenkins element with a variable normal load [23]. The contact element is uncoupled in two tangential x and y directions, where a representative view of a Jenkins element is shown in Figure 2a. The tangential friction force, T, can be calculated as

$$T_{x,y} = \begin{cases} \text{sign}(\dot{w}_{x,y})\mu N & \text{slip} \\ k_{t_{x,y}}(u_{x,y} - w_{x,y}) & \text{stick} \\ 0 & \text{separation} \end{cases}. \quad (8)$$

In Eq. (8), $\mu$ and $k_t$ are the coefficient of friction and tangential contact stiffness value, respectively. u and w represent the relative displacement in tangential direction and the slip motion of the slider, respectively. N is the variable normal load and can be computed as

$$N = \max(k_n v, 0), \quad (9)$$

where $k_n$ and v are the normal contact stiffness value and the relative displacement in normal direction, respectively. In this study, the complex amplitudes of contact forces are calculated by using the Alternating Frequency/Time (AFT) technique [24]. In this approach, first, the Inverse Discrete Fourier Transform (IDFT) is applied to the complex amplitude of the response to obtain time domain responses, and contact forces are calculated by using the Jenkins element. Then, contact forces computed in the time domain are transformed back to the frequency domain by utilizing Discrete Fourier Transform (DFT) to obtain complex amplitudes of the contact forces. The whole process is briefly shown in Figure 2b.

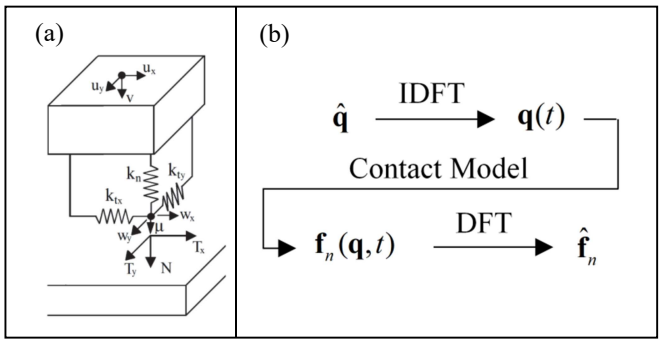


**FIGURE 2:** (a) CONTACT MODEL, (b) THE AFT METHOD

### 2.4 Receptance Notation and Partition of the Equations

Computational burden is one of the major problems in solving Eq.(5). Even though obtaining the ROM relieves it, further reduction may be possible with the use of receptance notation and by re-ordering the linear and nonlinear DOFs.

To avoid taking the inverse of system matrices in each iteration step of the solution procedure, Eq. (5) can be re-written with the receptance notation except for the $0^{\text{th}}$ harmonic as

$$\mathbf{K}^0\hat{\mathbf{q}}^0 + \hat{\mathbf{f}}_n^0 - \hat{\mathbf{f}}_{ex}^0 = \mathbf{0}$$
$$\hat{\mathbf{q}}^{eo\cdot h} + \boldsymbol{\alpha}^{eo\cdot h}\hat{\mathbf{f}}_n^{eo\cdot h} - \boldsymbol{\alpha}^{eo\cdot h}\hat{\mathbf{f}}_{ex}^{eo\cdot h} = \mathbf{0} \quad (h = 1, \cdots, H). \quad (10)$$

Here, the $0^{\text{th}}$ harmonic balance equations are left with the stiffness matrix, since receptance values for them are not defined due to free-free boundary conditions of the damper. $\boldsymbol{\alpha}^{eo\cdot h}$ is the receptance matrix corresponding to the $eo\cdot h^{\text{th}}$ harmonic and can be calculated without performing any inverse operation as

$$\boldsymbol{\alpha}^{eo\cdot h} = \sum_{r=1}^{N_m} \frac{\phi_r^{eo\cdot h}\left(\phi_r^{eo\cdot h}\right)^*}{\left(\omega_r^{eo\cdot h}\right)^2 - h^2\omega^2 + i2\xi_r^{eo\cdot h}h\omega\omega_r^{eo\cdot h}}. \quad (11)$$

In Eq.(11), $\phi_r^{eo\cdot h}$, $\omega_r^{eo\cdot h}$ and $\xi_r^{eo\cdot h}$ represent the mode shape, natural frequency and the proportional damping ratio for the

$r^{\text{th}}$ mode corresponding to the $eo \cdot h^{\text{th}}$ harmonics, respectively. $N_m$ denotes the number of modes considered in the expansion and it is equal to the number of DOFs of the ROM.

The contact forces also only depend on the nonlinear DOFs. Thus, Eq. (10) can be partitioned by linear (with subscription $l$) and nonlinear (with subscription $n$) DOFs as

$$\begin{bmatrix} \mathbf{K}_{ll}^0 & \mathbf{K}_{ln}^0 \\ \mathbf{K}_{nl}^0 & \mathbf{K}_{nn}^0 \end{bmatrix} \begin{Bmatrix} \hat{\mathbf{q}}_l^0 \\ \hat{\mathbf{q}}_n^0 \end{Bmatrix} + \begin{Bmatrix} \mathbf{0} \\ \hat{\mathbf{f}}_n^0 \end{Bmatrix} - \begin{Bmatrix} \hat{\mathbf{f}}_{ex,l}^0 \\ \hat{\mathbf{f}}_{ex,n}^0 \end{Bmatrix} = \mathbf{0}$$

$$\begin{Bmatrix} \hat{\mathbf{q}}_l^{eo\cdot h} \\ \hat{\mathbf{q}}_n^{eo\cdot h} \end{Bmatrix} + \begin{bmatrix} \boldsymbol{\alpha}_{ll}^{eo\cdot h} & \boldsymbol{\alpha}_{ln}^{eo\cdot h} \\ \boldsymbol{\alpha}_{nl}^{eo\cdot h} & \boldsymbol{\alpha}_{nn}^{eo\cdot h} \end{bmatrix} \begin{Bmatrix} \mathbf{0} \\ \hat{\mathbf{f}}_n^{eo\cdot h} \end{Bmatrix} - \begin{bmatrix} \boldsymbol{\alpha}_{ll}^{eo\cdot h} & \boldsymbol{\alpha}_{ln}^{eo\cdot h} \\ \boldsymbol{\alpha}_{nl}^{eo\cdot h} & \boldsymbol{\alpha}_{nn}^{eo\cdot h} \end{bmatrix} \begin{Bmatrix} \hat{\mathbf{f}}_{ex,l}^{eo\cdot h} \\ \hat{\mathbf{f}}_{ex,n}^{eo\cdot h} \end{Bmatrix} = \mathbf{0} \quad . \tag{12}$$

After separating the linear and nonlinear DOFs, the first set of equations can be utilized to define linear DOFs as

$$\begin{aligned} \hat{\mathbf{q}}_l^0 &= \left(\mathbf{K}_{ll}^0\right)^{-1} \left(\hat{\mathbf{f}}_{ex,l}^0 - \mathbf{K}_{ln}^0 \hat{\mathbf{q}}_n^0\right) \\ \hat{\mathbf{q}}_l^{eo\cdot h} &= \boldsymbol{\alpha}_{ll}^{eo\cdot h} \hat{\mathbf{f}}_{ex,l}^{eo\cdot h} + \boldsymbol{\alpha}_{ln}^{eo\cdot h} \left(\hat{\mathbf{f}}_{ex,n}^{eo\cdot h} - \hat{\mathbf{f}}_n^{eo\cdot h}\right) \quad \left(h = 1, \cdots, H\right) \end{aligned} \quad , \tag{13}$$

and then the final set of equations to be solved iteratively can be written for the nonlinear DOFs as

$$\begin{aligned} &\left(\mathbf{K}_{nn}^0 - \mathbf{K}_{nl}^0 \left(\mathbf{K}_{ll}^0\right)^{-1} \mathbf{K}_{ln}^0\right) \hat{\mathbf{q}}_n^0 + \mathbf{K}_{nl}^0 \left(\mathbf{K}_{ll}^0\right)^{-1} \hat{\mathbf{f}}_{ex,l}^0 + \hat{\mathbf{f}}_n^0 - \hat{\mathbf{f}}_{ex,n}^0 = \mathbf{0} \\ &\hat{\mathbf{q}}_n^{eo\cdot h} + \boldsymbol{\alpha}_{nn}^{eo\cdot h} \left(\hat{\mathbf{f}}_n^{eo\cdot h} - \hat{\mathbf{f}}_{ex,n}^{eo\cdot h}\right) - \boldsymbol{\alpha}_{nl}^{eo\cdot h} \hat{\mathbf{f}}_{ex,l}^{eo\cdot h} = \mathbf{0} \qquad \left(h = 1, \cdots, H\right) \end{aligned} \quad . \tag{14}$$

After obtaining the unknown response vector for nonlinear DOFs from Eq. (14), the response of linear DOFs can be easily obtained with Eq. (13) without performing any iteration.

### 2.5 Solution Procedure

In this study, the coupled set of Eq. (14) is solved simultaneously by using Newton-Raphson method with pseudo Arc-length Continuation [25]. In this approach, frequency is also another unknown in addition to the nonlinear DOFs. The main aim is to make the residual of Eq. (14) is zero, which can be written as

$$\mathbf{R}(\hat{\mathbf{q}}_n^{eo\cdot h}, \omega) = \mathbf{0} \qquad \left(h = 0, \cdots, H\right). \tag{15}$$

It is worth mentioning that the residual of the $0^{\text{th}}$ harmonic should be normalized in order to avoid a convergence problem. This is necessary, because the residual of the $0^{\text{th}}$ harmonic is defined in terms of force, while the one for the $eo \cdot h^{\text{th}}$ harmonics is in terms of displacement. Iterative formula for the current solution point is then written as

$${}_{j+1}\mathbf{Y} = {}_j\mathbf{Y} - \begin{bmatrix} \dfrac{\partial \mathbf{R}({}_j\mathbf{Y})}{\partial\, {}_j\hat{\mathbf{q}}_n^{eo\cdot h}} & \dfrac{\partial \mathbf{R}({}_j\mathbf{Y})}{\partial\, {}_j\omega} \\ \dfrac{\partial \mathbf{h}({}_j\mathbf{Y})}{\partial\, {}_j\hat{\mathbf{q}}_n^{eo\cdot h}} & \dfrac{\partial \mathbf{h}({}_j\mathbf{Y})}{\partial\, {}_j\omega} \end{bmatrix}^{-1} \times \begin{Bmatrix} \mathbf{R}({}_j\mathbf{Y}) \\ \mathbf{h}({}_j\mathbf{Y}) \end{Bmatrix}, \tag{16}$$

where

$${}_j\mathbf{Y} = \begin{Bmatrix} {}_j\hat{\mathbf{q}}_n^{eo\cdot h} \\ {}_j\omega \end{Bmatrix} \quad \text{and} \quad \mathbf{h}({}_j\mathbf{Y}) = \mathbf{Z}^T \left(\mathbf{Y}_p - {}_j\mathbf{Y}\right). \tag{17}$$

Here, subscript $j$, $\mathbf{Z}$ and $\mathbf{Y}_p$ represent the iteration number, the unit vector tangent to the solution curve and predicted unknown vector before starting iterations, respectively. $\mathbf{Y}_p$ can be estimated as

$$\mathbf{Y}_p = \mathbf{Y}_k + s\mathbf{Z}\,. \tag{18}$$

In Eq. (18), $\mathbf{Y}_k$ and $s$ represent the response vector converged at the previous solution point and the scalar arc-length parameter value that controls the length of the predictor, respectively.

## 3. RESULTS AND DISCUSSION

### 3.1 Modeling Approach

Finite element model of the fundamental sector is constructed by utilizing one of the commercial software. Linear solid elements are used with a total of 2.5 million DOFs approximately in the full model. The models are shown in Figure 3.

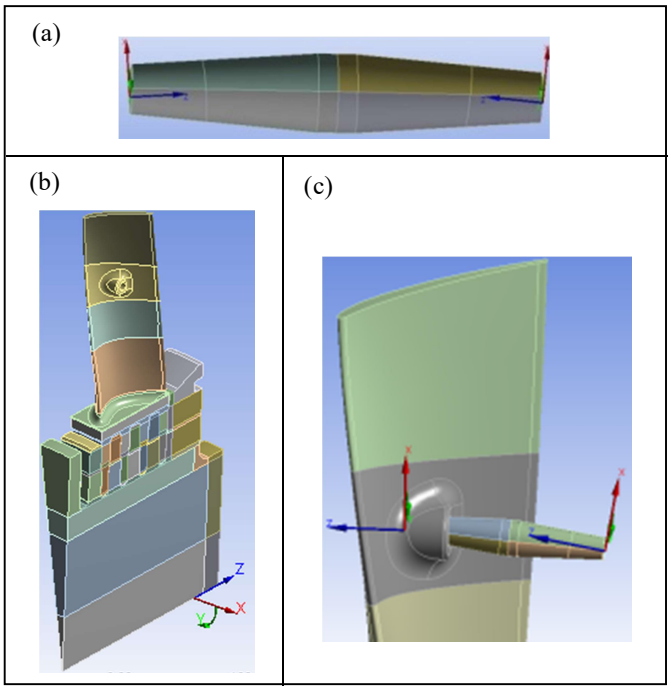


**FIGURE 3:** (a) DAMPER MODEL, (b) BLADE SECTOR MODEL, (c) ASSEMBLED VIEW. 

The material of the structures is steel with Young's modulus $E = 210$ GPa, Poisson coefficient $\nu = 0.3$ and

density $\rho = 7800$ kg/m$^3$. The MSD has a bi-conical shape, while the slots, where the damper penetrates into the blade, are cylindrical. Only some portion of the damper comes into contact with the blade pocket located approximately around 70% of the airfoil span. It should be noted that the friction damping generated at the blade root is neglected in this study and the blade–disk joint is modeled as perfectly linearly elastic.

The static pre-load that simulates the centrifugal force and keeps the damper in contact with the blade during operation is applied on the damper model at 5 different nodes along the damper axis, as shown in Figure 4a. With this type of static forcing, upper portion of the MSDs touches to the blade. The contact surfaces between the blade and damper are precisely meshed so that the contact nodes of the blade and damper in the slot overlap and couple the system through contact elements. It has been shown in [26] that wear is generally localized along a line for a cylindrical contact surface. In addition, based on the previous experience of Baker Hughes Company, the cylindrical surface typically restricts the contact patch to a very limited region on a line. Hence, a theoretical line contact with 31 pair nodes at each side is assumed in the analyses. Each pair node has two tangential directions in the circumferential and axial direction of the damper, while the normal direction is defined radially from the rotor hub. Contact lines are shown in Figure 4b with a section view.

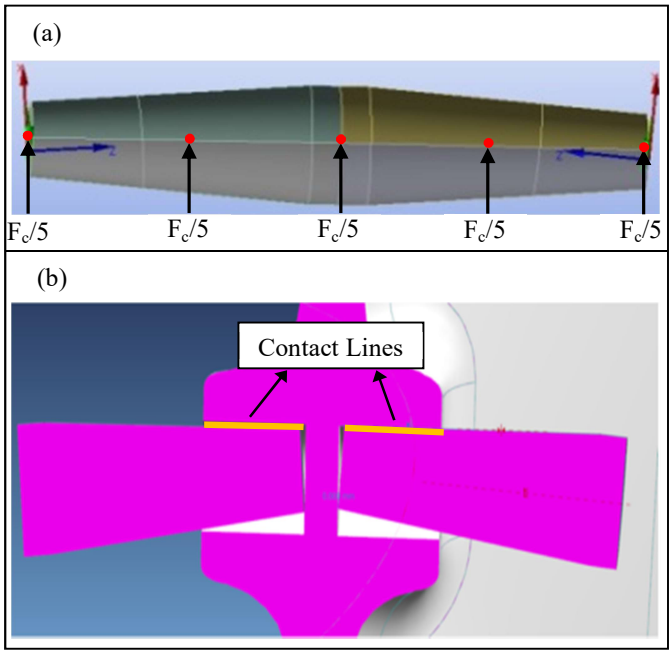


**FIGURE 4:** (a) STATIC PRE-LOAD ON THE DAMPER, (b) SECTION VIEW OF THE CONTACT REGION. 

Contact parameters play an important role on the dynamic characterization of dampers. Several studies have been performed in the last years [27-30] to correctly determine the contact properties. In this study, a numerical approach [29] is utilized to calculate the contact stiffness values. In this technique, the main principle of a flat indenter with rounded edges that is pressed onto an infinite half-space is used. However, since the contact surface is cylindrical in our case, the extent of the punch flat area is set equal to zero. It should be noted that contact stiffness values are directly dependent to centrifugal force in the turbomachinery applications. It increases with the rotor rotation speeding up, while it decreases with slowing down. Hence, it varies with different pre-load values. The overall contact stiffness value obtained for each surface is equally divided into number of contact nodes and shared by each contact element evenly. Eventually, the normal contact stiffness is obtained in the range of $1.24\times10^3$ – $1.76\times10^3$ N/mm for the normal direction, and the tangential contact stiffness value is computed within the range of $1.19\times10^3$ – $1.66\times10^3$ N/mm for the circumferential and axial directions. The coefficient of friction, $\mu$, is assumed 0.5 and kept constant throughout the numerical simulations.

Dynamic excitation force is distributed over the airfoil and applied at 19 different nodes as shown in Figure 5. Unit force is exerted to each node from the direction of the nozzle axis. Linear viscous damping is used and 1% proportional damping ratio is assumed. The 0$^{th}$ and the 1$^{st}$ harmonics are used in the coupled Harmonic Balance equations. Displacement amplitude of the blade tip is presented in the results.

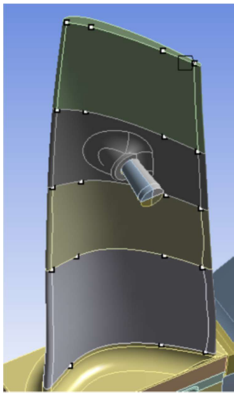

**FIGURE 5:** EXCITATION FORCE APPLICATION NODES. 

### 3.2 Dynamic Behavior of the Last Stage Blades with Mid-Span Dampers

Nonlinear response analyses are performed with the 6$^{th}$ engine order around the first four resonances. The first four mode shapes of the sector for the 6$^{th}$ harmonic index are given in Figure 6a-d, respectively. The first one is in-plane bending mode. The second one is a coupled mode of the damper and blade, while the third one is a torsional mode. The fourth one is another coupled mode of the torsional and out-of-plane bending.

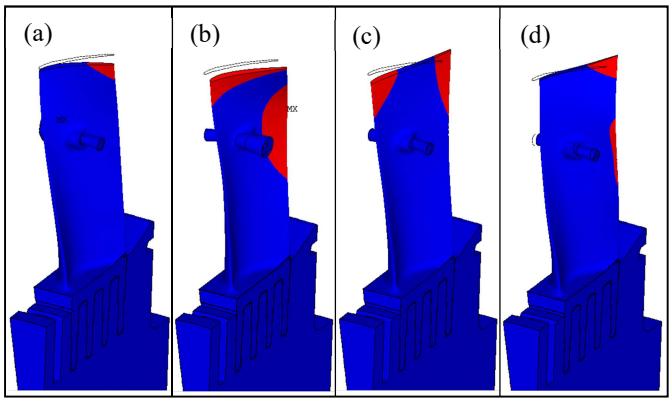


**FIGURE 6:** THE FIRST FOUR MODE SHAPES OF THE FUNDAMENTAL SECTOR FOR THE 6TH HARMONIC INDEX. *© 2020 Baker Hughes Company - All rights reserved*

Figure 7 shows the steady-state vibration response obtained with different pre-loads around the first resonance. X and Y axes of the graph are normalized with respect to the first linear natural frequency value and the maximum free linear response value, respectively. The damper clearly dissipates energy and reduces vibration amplitudes. The response behavior shifts from the free linear response to the fully stuck linear response with the increase of static pre-load value, as expected. It should be noted that the natural frequency value of the fully stuck linear case is considerably higher than the free linear one. The reason for this high stiffening effect is that MSD is placed approximately 70% above from the blade root, which affects the system dynamics considerably and makes the coupled system much stiffer. This property of MSDs is highly critical in terms of the damper effect on the blade dynamics due to the location of the damper. Moreover, for the nonlinear analysis with the lowest pre-load (the orange curve), resonance is obtained at a frequency that is smaller than the free linear natural frequency value. This shows for relatively low pre-loads that the damper mass is more dominant on the resonance value than the stiffness provided with the presence of the damper.

Contact maps give valuable information to visualize the partial slip behavior of the damper by monitoring the contact conditions. Figure 8a-f shows the contact states at six consecutive frequency points marked with black dots around $\omega = 1.7 \times \omega_n$ for a response curve that is close to fully stuck region of the first mode, i.e. blue response curve shown in Figure 7. A cross-section view of the upper line of the damper is simply visualized by highlighting the contact nodes with markers depending on the contact states. The red circle represents that the contact node is under fully stuck state, while the green stars indicate that there is an alternating stick-slip motion without separation during the cycle. Blue line in Figure 8 also represents the upper damper line that is not in contact with the blade. In this particular case, frequency sweep is performed from higher to lower values. Figure 8a is the contact map obtained at the first frequency just before slip starts, which means the damper is fully stuck. Figure 8b shows that partial slip initiates at the edge contact nodes for both sides and it is propagated through the inner nodes with progressing frequency values as can be seen in Figure 8c-f.

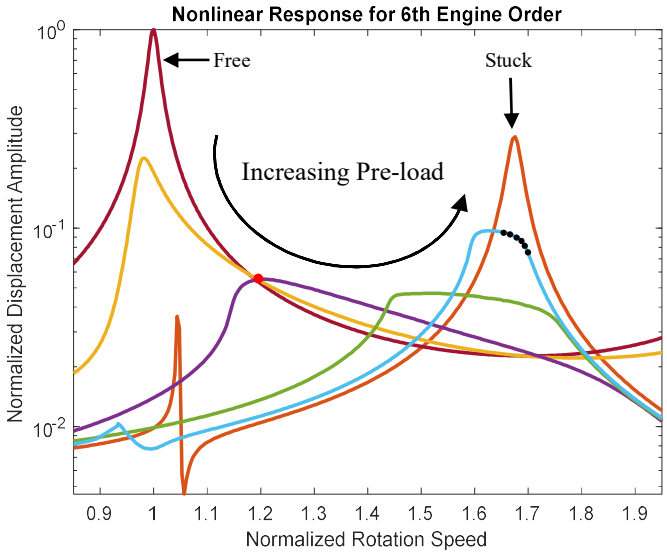


**FIGURE 7:** FREQUENCY RESPONSE CURVES AROUND THE 1ST RESONANCE WITH DIFFERENT PRE-LOADS. *© 2020 Baker Hughes Company - All rights reserved*

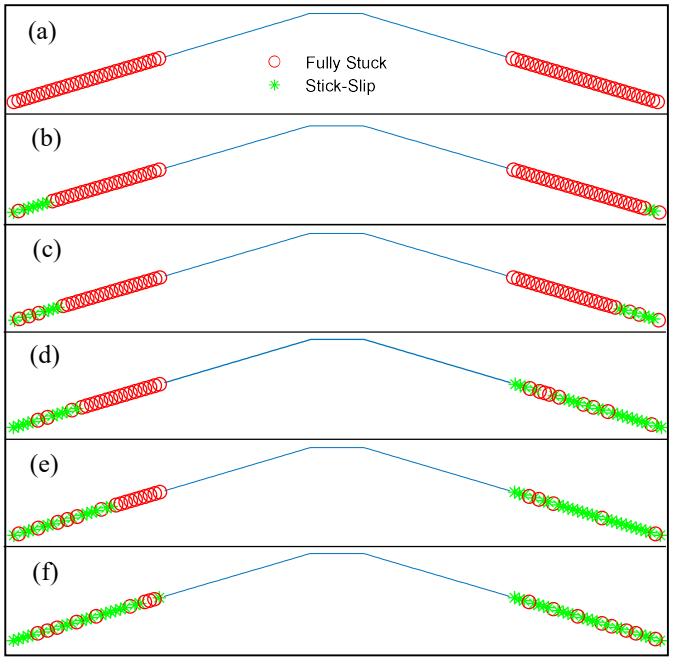


**FIGURE 8:** CONTACT CONDITIONS AT SIX CONSECUTIVE FREQUENCIES. *© 2020 Baker Hughes Company - All rights reserved*

The responses obtained for different excitation values with the same initial pre-load around the 1st resonance are also shown in Figure 9. It can be seen that the damper is completely stuck for relatively low excitation values. There is just a frequency shift for this particular case and no damping

supplied. The damper starts to slip and provides energy dissipation for the moderate excitation values. The MSDs are designed to operate in these regions, since most of the damping is achieved around these frequencies. The curves finally approach to the free linear case for the higher excitation values, in which the dissipation effect of the damper decreases.

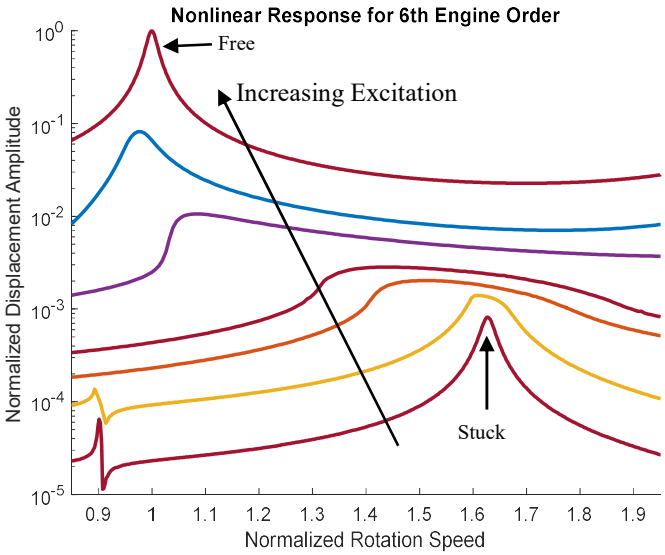


**FIGURE 9:** FREQUENCY RESPONSE CURVES AROUND THE 1ST RESONANCE WITH DIFFERENT EXCITATIONS. *© 2020 Baker Hughes Company - All rights reserved*

A similar response behavior is obtained around the 2nd resonance region, as shown in Figure 10. It is also interesting to note that the change of contact stiffness due to different pre-loads can be clearly seen by comparing the resonance frequencies of two response curves close to the fully stuck region. The resonance frequency of the fully stuck linear response curve is slightly larger than the other one; because the centrifugal force is higher in the former, which results in a larger contact stiffness value. The same observation is also valid in the first resonance region as can be seen in Figure 7. All the analyses show that MSDs work very well around the first two resonances to reduce the vibration amplitudes.

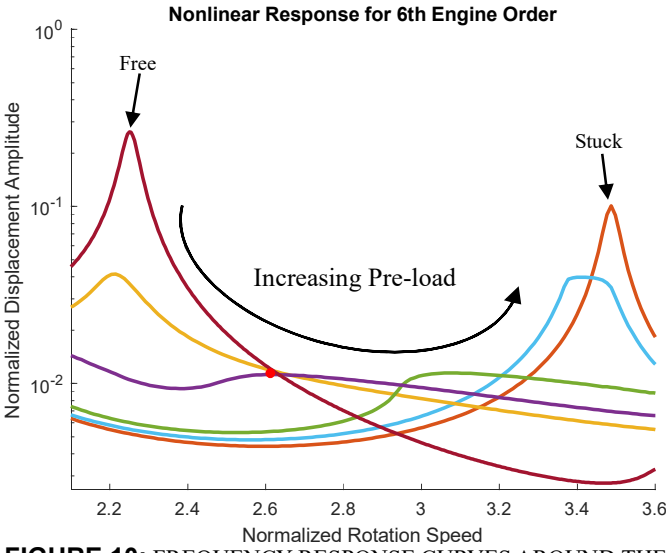


**FIGURE 10:** FREQUENCY RESPONSE CURVES AROUND THE 2ND RESONANCE WITH DIFFERENT PRE-LOADS. *© 2020 Baker Hughes Company - All rights reserved*

Vibration responses obtained with different pre-loads around the 3rd and the 4th resonances are also given in Figure 11. Similarly, the damper is capable of reducing the vibration amplitudes with friction for both resonance regions. It is interesting to note that although there is a stiffening effect for the 3rd resonance region, this observation is not valid for the 4th resonance region. On the contrary, the resonance frequency decreases due to the mass effect of the damper. This can be explained by the fact that the 4th mode of the sector (see Figure 6d) is a coupled mode of the torsional and out-of-plane bending, where the MSD and blade move together in the direction of out-of-plane. Thus, linear natural frequency of the free blade is not considerably affected by the presence of the damper, which prevents the stiffening effect.

Contact conditions during the energy dissipation for different resonances play an important role on the characterization of damper kinematics. In this study, contact maps are extracted at the frequency points marked with red dots on the purple response curves. These points are intentionally selected; because, purple curves are obtained with a relatively low pre-load under which the damper provides a large vibration reduction. Figure 12a-d illustrate the contact conditions at $\omega = 1.2 \times \omega_n$, $\omega = 2.6 \times \omega_n$, $\omega = 3.8 \times \omega_n$ and $\omega = 4.1 \times \omega_n$ for the first four resonance regions, respectively. Figure 12a and Figure 12b show that a stick-slip-separation motion takes place in some of the contact nodes around the first and the second resonances, respectively. Partial slip behavior is observed for all resonances at the left side of the damper, while all the nodes on the right side makes a stick-slip motion except the first resonance. All contact maps show that MSDs are an efficient type of dampers to reduce the vibration amplitudes of LSBs with a partial slip behavior.

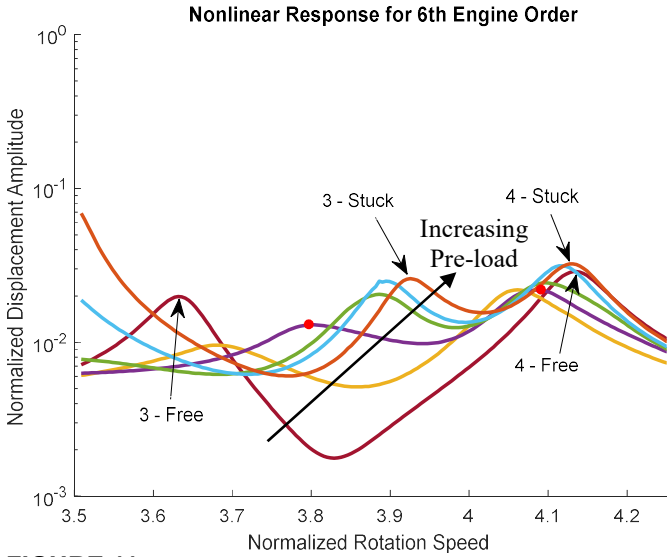


**FIGURE 11:** FREQUENCY RESPONSE CURVES AROUND THE 3RD AND THE 4TH RESONANCES WITH DIFFERENT PRE-LOADS. *© 2020 Baker Hughes Company - All rights reserved*

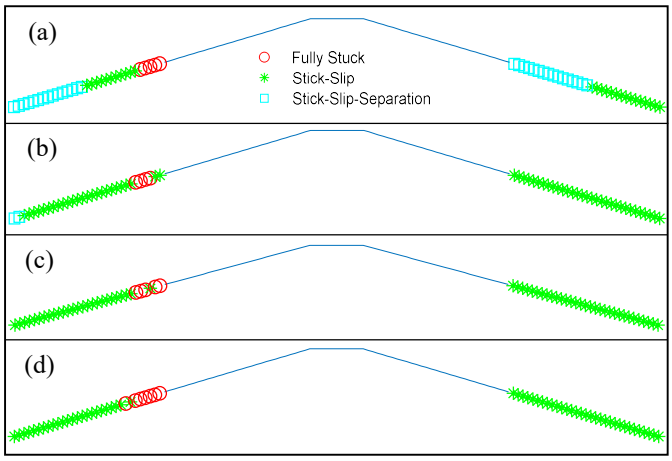


**FIGURE 12:** CONTACT CONDITIONS AT FOUR DIFFERENT RESONANCES. *© 2020 Baker Hughes Company - All rights reserved*

### 3.3 The Response Variability Phenomenon

Partial slip in friction dampers may result in multiple responses, even if all the inputs controlled by the user are kept identical [31]. It has been shown in [20] that the response variability can be related to an uncertainty present in the friction forces. For a simple illustration, consider a fully stuck contact element whose cycle is shown in Figure 13. According to the Coulomb's law, the tangential force is bounded by the upper and lower limits; however, its static component can take a set of value within a range of $T^0_{max}$ and $T^0_{min}$. This means that an infinite number of tangential contact forces is possible with the non-unique $T^0$ for a stuck element. Under the partial slip and the coupling between the two damper sides, different static balances can be obtained for the same nominal conditions. This phenomenon may change the dissipation ability of the damper and provide non-unique vibration responses. Experimental studies [32, 33] have also shown that the nonlinear response may vary considerably under the same nominal system parameters, due to non-uniqueness of the contact forces.

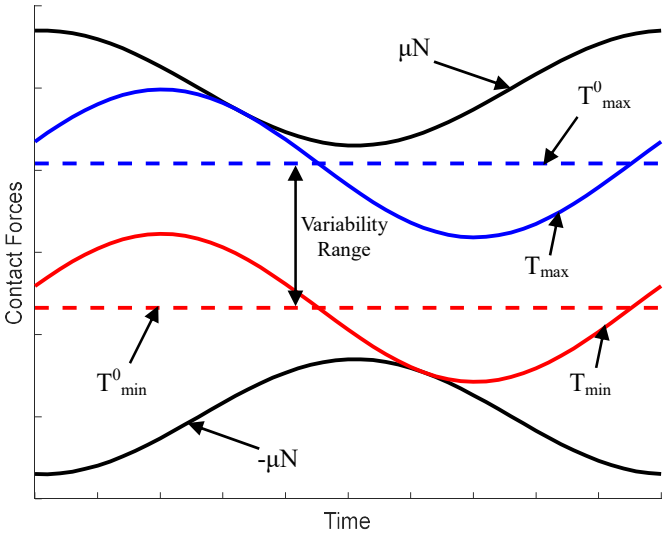


**FIGURE 13:** VARIABILITY OF THE TANGENTIAL FORCE FOR A FULLY STUCK CYCLE. *© 2020 Baker Hughes Company - All rights reserved*

In this study, the variability phenomenon is separately investigated in two particular cases with a low and a high pre-load. This allows identifying the kinematics of the variability under different conditions. The first case is examined with a relatively low pre-load, in which Figure 14 shows the response curves. The three nonlinear response curves are obtained by keeping all the system parameters exactly the same. The only difference between the analyses is the frequency step used during simulations. This provides the static tangential force component of fully stuck elements to change in each analysis; because, the nonlinear solver uses the converged results at the previous frequency point for the next one as an initial guess, which in turn, becoming a different one in each analysis. As a result, once the frequency points change in the analyses, different static balances on the damper and a non-unique response is achieved, although the inputs are identical.

It is clearly seen from Figure 14 that the response may vary significantly. For this specific example, the responses are obtained by sweeping the frequency from higher to lower. The same initial guess value is assigned at the very first frequency ( $\omega = 1.95 \times \omega_n$ ) in each analysis, which provided the same response value initially. However, the response curves are separated from each other after a certain frequency value, since different contact states are progressively achieved during the analyses. There is almost even ten times difference between the green and blue responses around $\omega = 1.15 \times \omega_n$ frequency value.

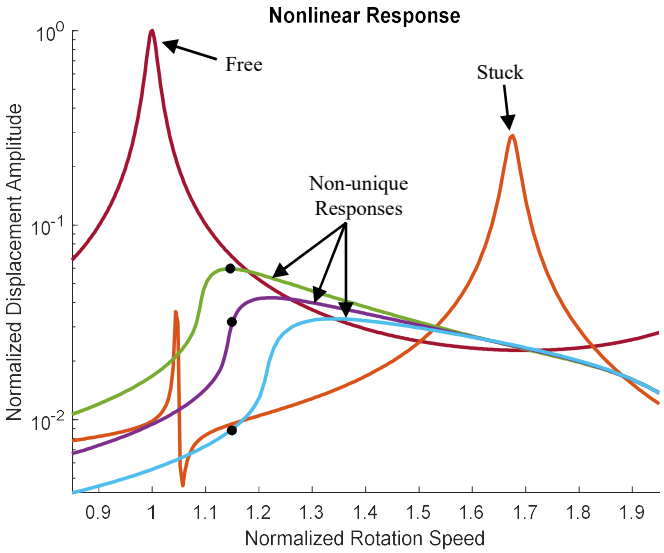


**FIGURE 14:** THE VARIABILITY OF THE FREQUENCY RESPONSE FOR A RELATIVELY LOW PRE-LOAD. 

In order to investigate the underlying kinematics of the variability, the contact states at frequency points marked in Figure 14 with black dots ($\omega = 1.15 \times \omega_n$) are studied. Figure 15a-c show the contact conditions for the green, purple and blue curves, respectively. It is seen that contact states at the same frequency are quite different in each case, although all the system parameters are kept same. The general pattern is similar, but non-unique tangential forces induced the contact states to propagate in a different way during the analyses. Partial slip is observed, as expected, since it is one of the main reasons for the variability. It is also interesting to note that the number of separating nodes in Figure 15a is higher than the other ones. This provides a loss of stiffness and the green curve to be closer to the free linear response than the other ones.

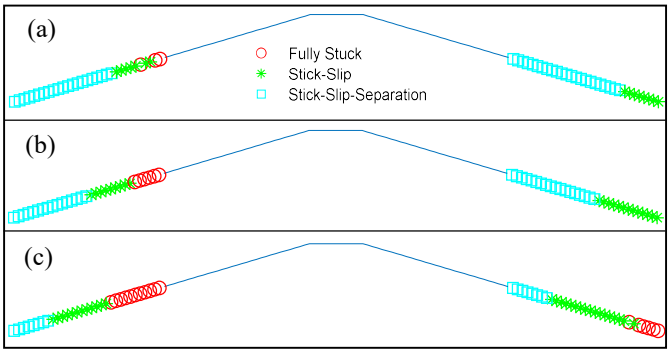


**FIGURE 15:** CONTACT CONDITIONS FOR THE NON-UNIQUE RESPONSE WITH A RELATIVELY LOW PRE-LOAD. 

The variability is also investigated with a higher pre-load. In this case, the non-unique nonlinear response is obtained close to the fully stuck linear one, as shown in Figure 16. It should be noted that the variability in the response is considerably smaller than the previous case and the curves almost overlap each other. The main reason of this fact can be better understood with the contact conditions. Figure 17a-c depicts the contact states for three curves around the resonance frequency marked with a black dot in Figure 16. The damper motion is dominated by an alternating stick-slip behavior on the contacts. Hence, the uncertainty in the friction forces highly decreases due to the fact that it is originated by the fully stuck contacts. An almost unique response is obtained and a small difference in contact states causes a slight variation in the response curves as can be seen in Figure 16. It can be inferred from all of the results that if the damper is in gross slip or fully stuck, the nonlinear response approaches an identical pattern and becomes unique. On the other hand, once the partial slip is high, the response may vary considerably in different analyses with the same system parameters.

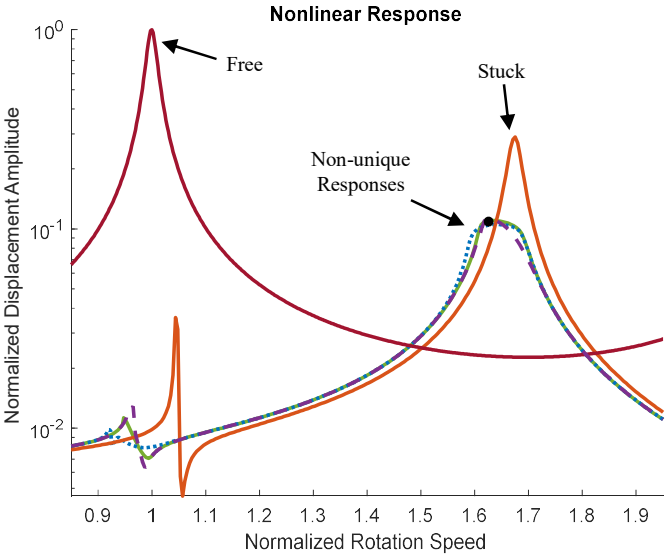


**FIGURE 16:** THE VARIABILITY OF THE FREQUENCY RESPONSE FOR A RELATIVELY HIGH PRE-LOAD. 

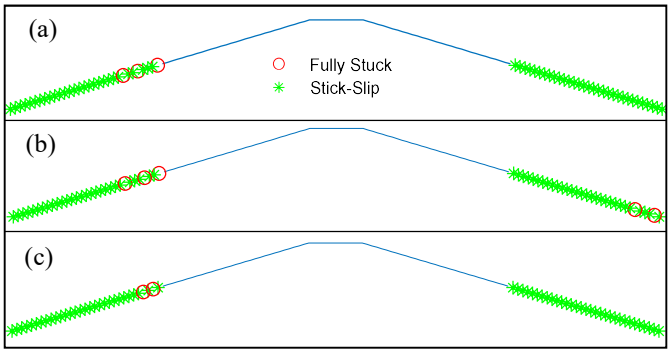


**FIGURE 17:** CONTACT CONDITIONS FOR THE NON-UNIQUE RESPONSE WITH A RELATIVELY HIGH PRE-LOAD. 

## 4. CONCLUSION

In this study, the nonlinear vibration analysis of a steam turbine bladed disk with a different configuration type of dampers, the so-called Mid-Span Damper (MSD), is investigated. Although this type of damper has been used by Baker Hughes Company for a while, this study presents the first intensive nonlinear dynamic characterization of MSDs with the coupled approach of static and dynamic equations in the solution procedure, to the best of authors' knowledge. It is shown in the numerical analyses that MSD greatly affects the dynamic behavior of the bladed disk and reduces the large vibration amplitudes effectively. The analyses are performed for various pre-loads and excitation levels around different resonance regions. It is concluded that MSDs has a high capability of dissipating the excessive energy with friction.

It is also shown for the first time that the nonlinear vibration response in the MSD applications may vary considerably under the same nominal conditions, due to an uncertainty related to the non-uniqueness of friction forces. The damper kinematics in different cases is shown by investigating the contact conditions. It is inferred that variability decreases when the damper approaches a gross slip motion. On the other hand, partial slip may allow obtaining a non-unique response and the variability can be extremely large.

## REFERENCES


[1] Cowles, B. A. "High Cycle Fatigue in Aircraft Gas Turbines - An Industry Prospective." *Int. J. Fracture* Vol. 80 No. 2-3 (1996): pp. 147–163.

[2] Srinivasan, A. V. "Flutter and Resonant Vibration Characteristics of Engine Blades." *ASME J. Eng. Gas Turbines Power* Vol. 119 No. 4 (1997): pp. 742–775.

[3] Petrov, E. P. and Ewins, D. J. "Effects of Damping and Varying Contact Area at Blade-Disc Joints in Forced Response Analysis of Bladed Disk Assemblies." *ASME J. Turbomach.* Vol. 128 No. 2 (2006): pp. 403-410.

[4] Charleux, D., Gibert, C., Thouverez, F. and Dupeux, J. "Numerical and Experimental Study of Friction Damping Blade Attachments of Rotating Bladed Disks." *Int. J. Rotating Mach.* Vol. 2006 (2006): Article ID. 71302.

[5] Petrov, E. P. and Ewins, D. J. "Analytical Formulation of Friction Interface Elements for Analysis of Nonlinear Multi-Harmonic Vibrations of Bladed Discs." *ASME J. Turbomach.* Vol. 125 No. 2 (2003): pp. 364-371.

[6] Siewert, C., Panning L., Wallaschek, J. and Richter C. "Multiharmonic Forced Response Analysis of a Turbine Blading Coupled by Nonlinear Contact Forces." *ASME J. Eng. Gas Turbines Power* Vol. 132 No. 8 (2010): 082501.

[7] Laxalde, D., Thouverez, F. and Lombard, J. P. "Forced Response Analysis of Integrally Bladed Disks with Friction Ring Dampers." *J. Vib. Acoustics* Vol. 132 No. 1 (2010): 011013.

[8] Tang, W., Epureanu, B.I. "Nonlinear Dynamics Of Mistuned Bladed Disks With Ring Dampers.", *Int. J. Nonl. Mech.* Vol. 97 (2017): pp. 30-40.

[9] Sanliturk, K.Y., Ewins, D. J. and Stanbridge, A. B. "Underplatform Dampers for Turbine Blades: Theoretical Modeling, Analysis and Comparison with Experimental Data." *ASME J. Eng. Gas Turbines Power* Vol. 123 No. 4 (2001): pp. 919-929.

[10] Cigeroglu, E., An, N. and Menq, C. H. "Forced Response Prediction of Constrained and Unconstrained Structures Coupled Through Frictional Contacts." *ASME J. Eng. Gas Turbines Power* Vol. 131 No. 2 (2009): 022505.

[11] Zucca, S., Firrone, C. M. and Gola, M. "Modeling Underplatform Dampers for Turbine Blades: A Refined Approach in the Frequency Domain." *J. Vib. Control* Vol. 19 No. 7 (2012): pp. 1087-1102.

[12] Pesaresi, L., Armand, J., Schwingshackl, C. W., Salles, L. and Wong, C. "An Advanced Underplatform Damper Modelling Approach Based on a Microslip Contact Model." *J. Sound Vib.* Vol. 436 (2018): pp. 327–340.

[13] Yamashita, Y., Shiohata, K., Kudo, T. and Yoda, H. "Vibration Characteristics of a Continuous Cover Blade Structure with Friction Contact Surfaces of a Steam Turbine." *10th International Conference on Vibrations in Rotating Machinery*: pp. 323-332. IMechE London, UK, September 11-13, 2012.

[14] Drozdowski, R., Völker, L., Häfele, M. and Vogt, D. M. "Numerical and Experimental Analysis of Low-Pressure Steam Turbine Blades Coupled with Lacing Wire." *Proceedings of the Institution of Mechanical Engineers, Part A: Journal of Power and Energy* Vol. 230 No. 3 (2016): pp. 332-342.

[15] Szwedowicz, J., Secall-Wimmel, T. and Dünck-Kerst, P. "Damping Performance of Axial Turbine Stages with Loosely Assembled Friction Bolts: The Nonlinear Dynamic Assessment." *ASME J. Eng. Gas Turbines Power* Vol. 130 No. 3 (2008): 032505.

[16] Drozdowski, R., Völker, L., Häfele, M. and Vogt, D. M. "Experimental and Numerical Investigation of the Nonlinear Vibrational Behavior of Steam Turbine Last Stage Blades with Friction Bolt Damping Elements." *Proceedings of ASME Turbo Expo 2015: Turbine Technical Conference and Exposition*. Montreal, Canada, June 15-19, 2015.

[17] Voldřich, J., Lazar J. and Polach P. "Nonlinear Vibration Analysis of Steam Turbine Rotating Wheel Equipped with the LSB48 Blades." *The 14th IFToMM World Congress*: pp. 48-55. Taipei, Taiwan, October 25-30, 2015.

[18] Siewert, C., Sieverding, F., McDonald, W. J., Kumar, M. and McCracken, J. R. "Development of a Last Stage Blade Row Coupled by Damping Elements: Numerical Assessment of Its Vibrational Behavior and Its Experimental Validation During Spin Pit Measurements." *Proceedings of ASME Turbo Expo 2017: Turbomachinery Technical Conference and Exposition*. Charlotte, NC, USA, June 26-30, 2017.

[19] Firrone, C. M., Zucca, S. and Gola, M. M. "The Effect of Underplatform Dampers on the Forced Response of Bladed Disks by A Coupled Static/Dynamic Harmonic Balance Method." *Int. J. Non-linear Mech*. Vol. 46 No. 2 (2011): pp. 363-375.

[20] Ferhatoglu, E., Zucca, S. "On the Non-Uniqueness of Friction Forces and the Systematic Computation of Dynamic Response Boundaries for Turbine Bladed Disks with Contacts." *Mech. Syst. Signal Proc*. Vol. 160 (2021): 107917.

[21] Petrov, E. P. "A Method for Use of Cyclic Symmetry Properties in Analysis of Nonlinear Multiharmonic Vibrations of Bladed Disks." *ASME J. Turbomach.* Vol. 126 No. 1 (2004): pp. 175-183.

[22] Craig, R. R. and Bampton, M. C. C. "Coupling of Substructures for Dynamic Analyses." *AIAA J.* Vol. 6 No. 7 (1968): pp. 1313-1319.

[23] Jenkins, G.M. "Analysis of the Stress–Strain Relationships In Reactor Grade Graphite." *Br. J. Appl. Phys.* Vol. 13 No. 1 (1962): pp. 30.

[24] Cameron, T. M. and Griffin, J. H. "An Alternating Frequency/Time Domain Method for Calculating the Steady-State Response of Nonlinear Dynamic Systems." *J. Appl. Mech.* Vol. 56 No. 1 (1989): pp. 149-154.

[25] Chan, T. F. C. and Keller, H. B. "Arc-Length Continuation and Multigrid Techniques for Nonlinear Elliptic Eigenvalue Problems." *SIAM J. Sci. and Stat. Comput.* Vol. 3 No. 2 (1982): pp. 173–194.

[26] Zucca, S., Berruti, T. and Cosi, L. "Experimental and Numerical Investigations on the Dynamic Response of Turbine Blades with Tip Pin Dampers." *J. Physics: Coneference Series* Vol. 744 No. 1 (2016): 012131.

[27] Lavella, M., Botto, D. and Gola, M. M. "Fretting Wear Characterization by Point Contact of Nickel Superally Interfaces." *Wear* Vol. 271 No. 9-10 (2011): pp. 1543-1551.

[28] Schwingshackl, C. W., Petrov, E. P. and Ewins, D. J. "Measured and Estimated Friction Interface Parameters In a Nonlinear Dynamic Analysis." *Mech. Syst. Signal Proc*. Vol. 28 (2012): pp. 574-584.

[29] Allara, M. "A Model for the Characterization of Friction Contacts In Turbine Blades." *J. Sound Vib.* Vol. 320 No. 3 (2009): pp. 527-544.

[30] Stingl, B., Ciavarella, M. and Hoffmann, N. "Frictional Dissipation in Elastically Dissimilar Oscillating Hertzian Contacts." *Int. J. Mech. Sciences* Vol. 72 (2013): pp. 55-62.

[31] Yang, B. D. and Menq, C. H. "Characterization of Contact Kinematics and Application to the Design of Wedge Dampers in Turbomachinery Blading: Part 2—Prediction of Forced Response and Experimental Verification." *ASME J. Eng. Gas Turbines Power* Vol. 120 No. 2 (1998): pp. 418-423.

[32] Botto, D. and Umer, M. "A Novel Test Rig to Investigate Under-Platform Damper Dynamics." *Mech. Syst. Signal Proc*. Vol. 100 (2018): pp. 344-359.

[33] Gastaldi, C., Gross, J., Scheel M., Berruti, T. M. and Krack, M. "Modeling Complex Contact Conditions and Their Effect On Blade Dynamics." *ASME J. Eng. Gas Turbines Power* Vol. 143 No. 1 (2021): 011007